PAPER

ECH effects on toroidal rotation: KSTAR experiments, intrinsic torque modelling and gyrokinetic stability analyses

View the <u>article online</u> for updates and enhancements.

ECH effects on toroidal rotation: KSTAR experiments, intrinsic torque modelling and gyrokinetic stability analyses

Y.J. Shi[1,2]**, W.H. Ko**[2]**, J.M. Kwon**[1]**, P.H. Diamond**[1,3]**, S.G. Lee**[2]**,
S.H. Ko**[1]**, L. Wang**[4]**, S. Yi**[1]**, K. Ida**[5]**, L. Terzolo**[2]**, S.W. Yoon**[2]**,
K.D. Lee**[2]**, J.H. Lee**[2]**, U.N. Nam**[2]**, Y.S. Bae**[2]**, Y.K. Oh**[2]**, J.G. Kwak**[2]**,
M. Bitter**[6]**, K. Hill**[6]**, O.D. Gurcan**[7]** and T.S. Hahm**[8]

[1] WCI Center for Fusion Theory, National Fusion Research Institute, Daejeon 305–333,
Korea
[2] KSTAR, National Fusion Research Institute, Daejeon 305–333, Korea
[3] CMTFO and CASS, University of California, San Diego, CA 92904, USA
[4] College of Electrical and Electronic Engineering, Huazhong University of Science and
Technology, Wuhan 430074, People's Republic of China
[5] National Institute for Fusion Science, Toki, GiFu 509–5292, Japan
[6] Princeton Plasma Physics Laboratory, Princeton, NJ 08543-0451, USA
[7] Ecole Polytechnique, CNRS, Palaiseau Cedex 91128, France
[8] Department of Nuclear Engineering, Seoul National University, Seoul 151–742, Korea

E-mail: yjshi@nfri.re.kr

Abstract

Toroidal rotation profiles have been investigated in KSTAR H-mode plasma using combined auxiliary heating by co-neutral beam injection (NBI) and electron cyclotron resonance heating (ECH). The ion temperature and toroidal rotation are measured with x-ray imaging crystal spectroscopy and charge exchange recombination spectroscopy. H-mode plasma is achieved using co-current 1.3 MW NBI, and a 0.35 MW ECH pulse is added to the flat-top of H-mode. The core rotation profiles, which are centrally peaked in the pure NBI heating phase, flatten when ECH is injected, while the edge pedestal is unchanged. Dramatic decreases in the core toroidal rotation values ($\Delta V_{tor}/V_{tor} \sim -30\%$) are observed when on-axis ECH is added to H-mode. The experimental data show that the decrease of core rotation velocity and its gradient are correlated with the increase of core electron temperature and its gradient, and also with the likely steepening of the density gradient. We thus explore the viability of a hypothesized ITG (ITG ion temperature gradient instability) $\rightarrow$ TEM (trapped electron mode instability) transition as the explanation of the observed counter-current flow induced by ECH. However, the results of linear microstability analyses using inferred profiles suggest that the TEM is excited only in the deep core, so the viability of the hypothesized explanation is not yet clear.

(Some figures may appear in colour only in the online journal)

1. Introduction

Flow and velocity shear are very important for stabilizing micro- and macro-instabilities in tokamak plasmas. Neutral beam injection (NBI) is generally used as the external momentum input source to produce and control plasma rotation in present day tokamaks. For ITER and future reactors, the input torque from NBI will be very low or nonexistent and cannot produce the needed rotation. As a result, there is a need to develop alternative or complementary methods for driving plasma rotation. Significant intrinsic rotation (without external momentum input) has been observed on many tokamaks [1], which suggest that it may be possible to reap the benefits of such self-generated flows in ITER and reactors.

Since the discovery of intrinsic rotation in the 1990s [2, 3], plasma rotation without external torque has been a topic of intense interest. While significant progress has been made, the driving mechanisms are not fully understood. Theoretical models have been proposed to explain intrinsic rotation as due to a turbulence-driven intrinsic torque [4–7]. Intrinsic torque is dynamic and variable—due to evolving turbulent Reynolds stresses. Momentum transport bifurcations and reversals have

been observed in several experiments [8, 9]. The effects on toroidal rotation of electron cyclotron resonance heating (ECH) have being observed previously in CHS [10], DIII-D [11], JT-60U [12] and AUG [13, 14]. The counter-current rotation increment or flattening of co-current rotation profile was confirmed in these ECH experiments. The proposed explanations vary considerably. The KSTAR results in this paper, though partly similar to some previous experiments, will be combined with gyrokinetic stability analyses to elucidate possible physics mechanisms for ECH rotation experiments. In KSTAR H-mode, a core counter-current flow develops when ECH is injected. The pedestal is unchanged. KSTAR results suggest that toroidal rotation profiles in H-mode are determined by the interplay of (i) a core co-current NBI torque, (ii) a pedestal intrinsic torque, which is co-current, (iii) a core intrinsic torque, which becomes counter-current with the addition of ECH. Here, we investigate the hypothesis that the appearance of the core counter-current intrinsic torque with ECH is due to a transition from a state of ion temperature gradient (ITG) turbulence to a state of trapped electron mode (TEM) turbulence, and thus a change in the sign of the turbulence-driven residual stress [4, 7]. This mechanism is very similar to that invoked for explaining the phenomenon of OH rotation direction reversals, where an increase in density triggers a confinement transition (LOC → SOC), the transition from TEM to ITG, and thus a change in sign of the predicted residual stress. In the core plasma of KSTAR, the ITG → TEM transition might be triggered by the steepening of ∇T_e, the peaking of ∇n_e, and the drop in ν_{e*} due to the addition of ECH. The key role of ∇n_e evolution highlights the point that particle and momentum transport are strongly coupled.

This paper is organized as follows: an introduction to the experiment setup in KSTAR is given in section 2, which presents heating schemes, diagnostics and relevant plasma parameters. The main experimental results are described in section 3. Section 4 gives the analysis and interpretation of the effect of on-axis ECH heating plasma on toroidal rotation profiles in H-mode plasma. Conclusions and future plans are summarized in section 5.

2. Experimental setup

All the experimental results presented in this paper were obtained in the KSTAR superconducting tokamak [15]. Two diagnostics on KSTAR can measure the impurity ion rotation, temperature and brightness profiles. One is the x-ray imaging crystal spectroscopy (XICS) [16], which is a passive diagnostic and can provide nearly full-time information for all discharges using argon gas-puffing. The limitation of XICS in KSTAR is that only the core plasma is covered by XICS. The other diagnostic is the charge exchange recombination spectroscopy (CES) [17], which has 32 toroidal lines of sight and can provide the whole plasma profile from the plasma edge to the magnetic axis. CES in KSTAR needs NBI modulation to subtract the background signal and so CES can provide data for only a limited range of time. He-like argon spectra were used for XICS. The XICS on KSTAR cannot do absolute wavelength calibration itself. We use CES as the reference. In some discharges, locked-modes are also be used to calibrate XICS.
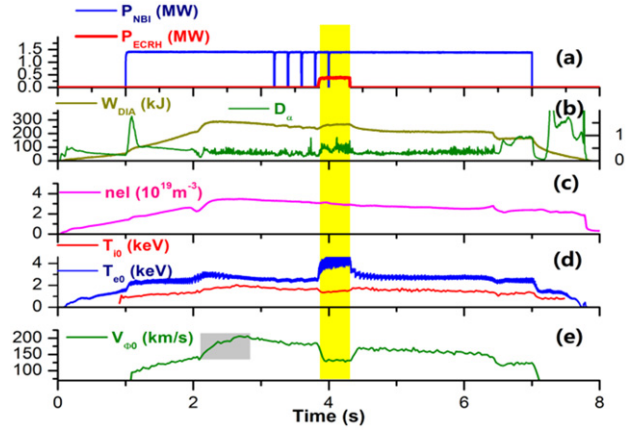

Figure 1. Time traces of the main parameters for H-mode discharge (sn5737) on KSTAR. ECH is injected on the flat-top of H-mode. (*a*) Power of NBI and ECH, (*b*) stored energy W_{dia} and D_α intensity, (*c*) central line-averaged density, (*d*) core electron and ion temperature, (*e*) core rotation velocity.

For present XICS on KSTAR, it is very difficult to do inversion due to the limited observation region. So the results of XICS in this paper are line-integrated. At the same time, we have done some simulation for the peaking emissivity profiles of XICS which shows that the difference between inverted results and line-integrated result is only about 10%. The temporal performance of XICS and full-spatial capacity of CES are complementary to each other. For the discharges where both XICS and CES can obtain data, there is good agreement of the core rotation velocity profiles from the two diagnostics. Thus, the rotation data presented here combines the results of XICS and CES. Electron temperature was measured with an electron cyclotron emission radiometer (ECE) [18]. The line-averaged density measurements are based on micro-wave interferometry and thus give indications of only the line-averaged values. Thomson scattering data is not yet available for the discharges in this paper.

The main plasma parameters in this paper are $I_p = 0.6$ MA, $B_T = 2$ T. Discharges were operated in double or quasi-double null configuration. The plasma elongation factor is about 1.8–1.9. The edge safety factor (q_{95}) is about 6.5 during H-mode phase. NBI is the main heating power in KSTAR. On-axis 1.2–1.4 MW NBI (90–95 keV) [19] were always injected in the co-current direction during the flap-top in the discharges presented here. There are two ECH heating system in KSTAR [20]. One is 110 GHz (source power 0.5 MW) and the other is 170 GHz (source power 1 MW). The ECH system was configured for X-mode second harmonic @ 110 GHz or third harmonic @ 170 GHz and deposition location was set using steerable mirrors. The toroidal angle of ECH is almost perpendicular to the magnetic field such that the current-driven effect can be neglected.

3. Experimental results

One typical set of waveforms for combined auxiliary heating of NBI and ECH is shown in figure 1. 1.3 MW NBI was injected from 1.0 to 7.0 s and was sustained during the major part of the discharge pulse. H-mode plasma was achieved at
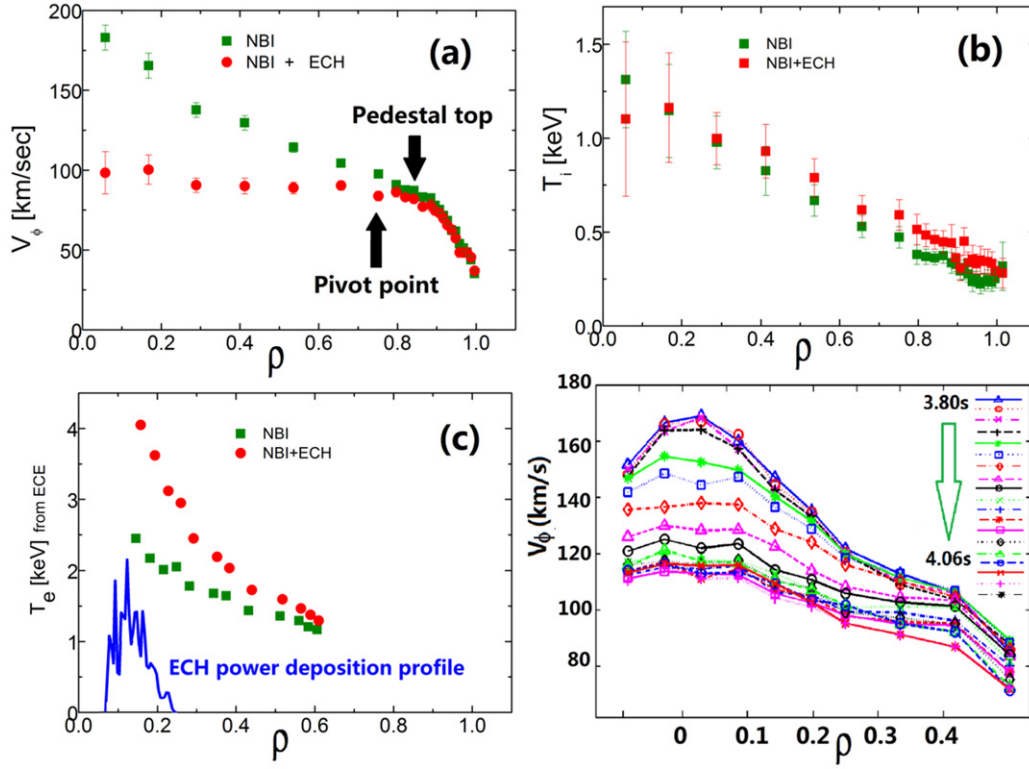
Figure 2. (*a*) Profiles of rotation by CES, (*b*) ion temperature by CES, (*c*) electron temperature by ECE and power deposition profile of ECH, (*d*) time evolution of rotation profiles by XICS (from 3.8 to 4.05 s) during injection of ECH (time resolution is 14 ms).

2.1 s and sustained to 6.5 s by NBI, which is clearly indicated by the increment of stored energy and the D_α ELM signal. The centre line-averaged density was about $2.5 \times 10^{19}\,\mathrm{m^{-3}}$ before L–H transition and increased to $3.4 \times 10^{19}\,\mathrm{m^{-3}}$ after L–H transition. The core rotation also increased by about $80\,\mathrm{km\,s^{-1}}$ after the L–H transition. A 0.5 s duration pulse of 350 kW on-axis ECH was added at 3.84 s in the steady-state phase of H-mode plasma. Many parameters responded to the injection of ECH. The core electron temperature and its gradient increased significantly due to the direct on-axis heating by ECH (as shown in figure 2(*c*)). Plasma stored energy also increased about 13%. The core ion temperature decreased slightly (about 11%). At the same time, the core toroidal rotation dramatically decreased by 30%. Figure 2 shows the rotation profile for NBI phase and ECH phase from XICS and CES. The results from each of the two diagnostics clearly show the peaked rotation profiles in NBI phase evolve to flat profiles after injection of ECH. Note the region of change, i.e. $\rho < \rho_{pv} \sim 0.7$ where ρ_{pv} is the point about which the profile pivots in figure 2(*a*), clearly lies within the core, and does not overlap the pedestal (i.e. $\rho_{pv} < \rho_{ped}$, where ρ_{ped} is the position of the top of the pedestal). The pedestal rotation is unchanged. Figure 2(*d*) shows the detailed time traces of rotation velocity at different positions during the ECH phase, which show that the response of rotation at $\rho = 0$ to ECH is faster than that of the rotation at $\rho = 0.5$. The profiles of ion temperatures are shown in figure 2(*b*) (CES measurement) and figure 4(*b*) (XICS measurement). The slight reduction of T_i in core region and tiny increase of T_i in outer can be observed during injection of ECH both from CES and XICS. Modification of ion thermal diffusivity is one possible reason
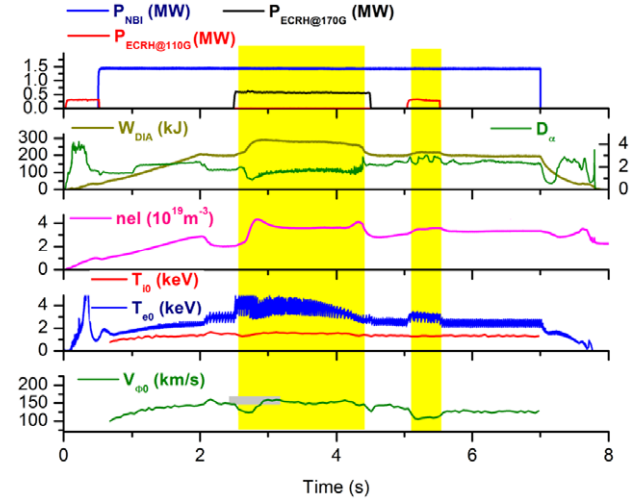

Figure 3. Time traces of the main parameters for another H-mode discharge (sn6384). The signals are the same as those in figure 1.

for the change in ion temperature profile. The significant decrease in core rotation cannot be explained by a simple increase of momentum diffusivity [13] and the slight decrease of ion pressure gradient or by a change in the beam torque. From figures 1 and 2, we see that the change in rotation is correlated with the increase in the electron temperature gradient.

Figure 3 shows the results for different waveforms of on-axis ECH and NBI heating. Two 110 GHz ECH pulses were injected at startup (0–0.5 s) and flat-top (5–5.5 s) in the L-mode phase. A 170 GHz ECH pulse covered both L-mode
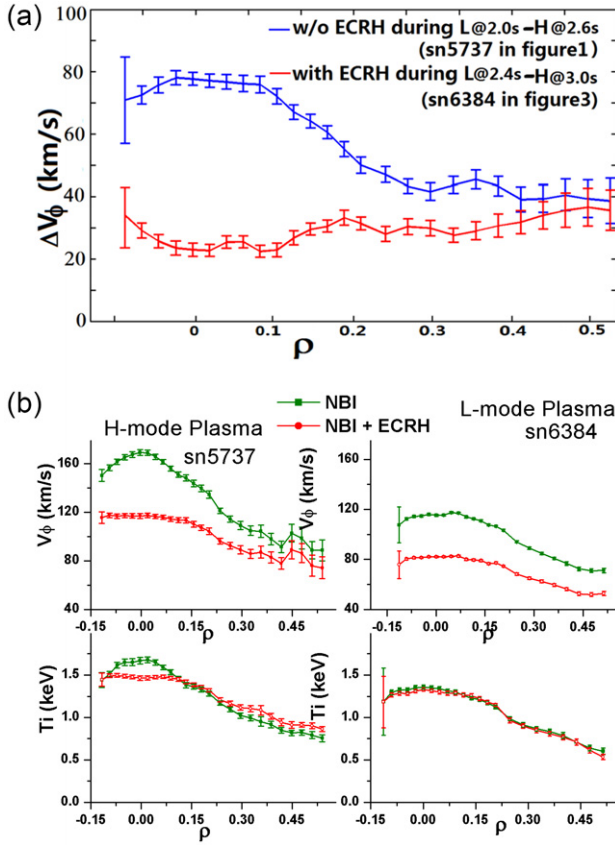
3

Figure 4. (*a*) The profiles of rotation increment (measured with XICS). (*b*) The profiles of rotation (up) and ion temperature (low) for two ECH cases (measured with XICS).

Figure 5. Cartoon showing three torques for ECH + NBI H-mode plasma.

and H-mode phases from 2.5 to 4.5 s in this shot. H-mode plasma was initiated at around 2.65 s with the combination heating of NBI and 170 GHz ECH and return to L-mode at about 4.4 s. After the injection of ECH, the core temperature and stored energy increased. The toroidal rotation dropped markedly in both the 110 GHz ECH L-mode phase (5–5.5 s) and 170 GHz ECH L-mode phase (2.5–2.65 s). Although, the power of the 170 GHz ECH is much higher than of the 110 GHz ECH, the decrease of rotation velocity was almost the same for the two heating L-mode phases. The reason is likely that the heating efficiency of 170 GHz EC waves at third harmonic is much lower than that of 110 GHz EC waves at second harmonic. On the other hand, the increment of core rotation $\Delta V(r) = V_H(r) - V_L(r)$ due to the L–H transition in this discharge is much lower than for the pure NBI-induced H-mode plasma in figure 1 (The profiles of the increment for the two cases are shown in figure 4(*a*)), where $V_H(r)$ is rotation velocity in H-mode flat-top phase, $V_L(r)$ is the rotation velocity in L-mode phase without ECH heating. The exact time for $V_H(r)$ and $V_L(r)$ are shown in figure 4(*a*). Because we have no effective CES for the discharge in figure 3, only core profiles from XICS were shown in figure 4. It can be seen that the increment in rotation is almost the same in the outer plasma, while the core rotation increment for pure NBI achieved in H-mode is much higher than that with ECH injection. The peaked increment profile of rotation in figure 4(*a*) is caused mainly by the co-current intrinsic torque driven by the H-mode pedestal with the assistance of the pinch effect [21]. When
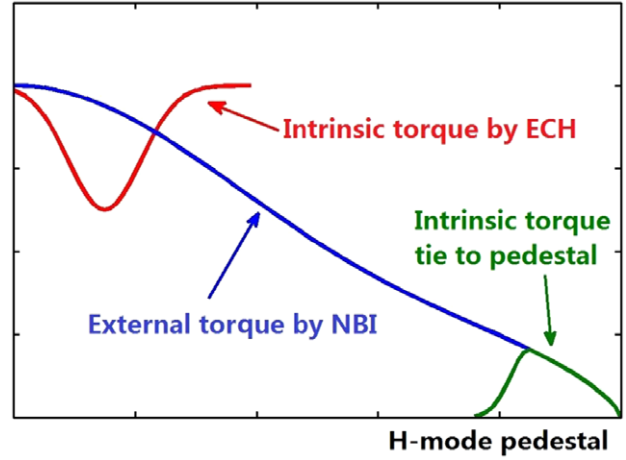
ECH is injected during H-mode, the core counter-current intrinsic torque opposes the effect of the pedestal co-current intrinsic torque. The flat increment profile in figure 4(*a*) is then the result of the balance between two torques. When ECH is injected into L-mode plasma (as shown in figure 4(*b*)), we note that the ECH-induced intrinsic torque has the same direction (i.e. the counter-current direction) at similar radial position in both L and H-mode, though there would be some variations in the strength of the torque. On the other hand, rotation decreases over a broad spatial range when ECH is injected into L-mode plasma (as shown in figure 4(*b*)). In figure 4(*b*), the ratio of rotation reduction between $\rho = 0.5$ and $\rho = 0$ due to ECH in L-mode is about 0.67 $\left(\frac{20\,\mathrm{km\,s^{-1}}\,(\rho=0.5)}{30\,\mathrm{km\,s^{-1}}\,(\rho=0)} \right)$, which is much higher than that value $\left(\frac{12\,\mathrm{km\,s^{-1}}\,(\rho=0.5)}{50\,\mathrm{km\,s^{-1}}\,(\rho=0)} \right)$ in H-mode case. A likely reason is that the effects of the counter-current torque can easily spread to larger radii without opposition from a pedestal intrinsic torque. As shown in simple cartoon in figure 5, the co-current external NBI torque is the dominate power to decide the basic rotation profile in KSTAR. Then, the counter-current intrinsic torque by ECH and the co-counter intrinsic torque tie to pedestal modify the rotation profile, further. The comparison between rotation profiles for two kinds of L–H transition (with ECH and without ECH during L–H) and L-mode and H-mode ECH plasma demonstrate that the rotation profiles for ECH + NBI H-mode plasma are determined by the three way competition between the core co-NBI torque, the pedestal intrinsic co-torque, and the core ECH-induced counter-torque.

Considerable insight may be gleaned by consideration of macroscopic correlations. Of course, these are only correlations and do not establish causality. The first pair of plots in figure 6 shows a plot of $-\Delta V_\phi$ (change in V_ϕ due to ECH) versus ΔT_e, the change in the central electron temperature. A linear scaling relation is apparent. Note that this is the ECH analogue of a 'Rice scaling' ($\Delta V_\phi \sim \Delta W/I_p$) and gives the relation between the increment of reduction in V_ϕ and the increase in electron temperature. The second pair of figures in figure 6 show the correlation between the change in $-dT_e/dr$ (i.e. compare NBI points with NBI + ECH points) and dV_ϕ/dr. The trend showing that steepening of dT_e/dr is
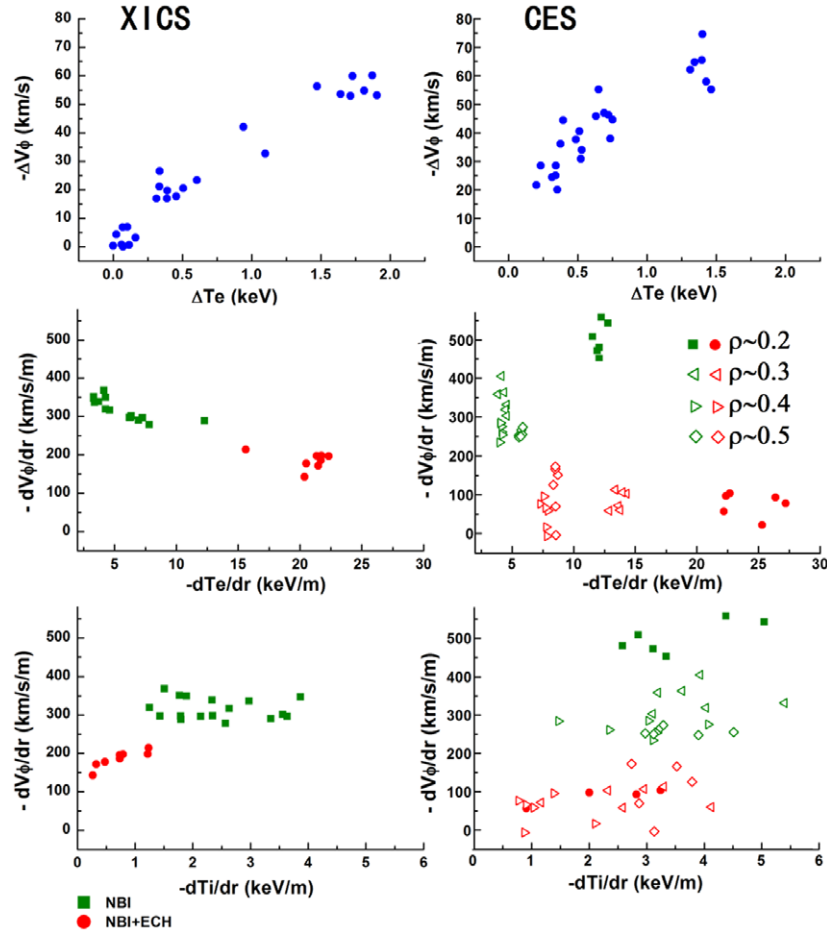
Figure 6. The correlation between $\Delta V\phi$ and ΔT_e (top), $\nabla V\phi$ and ∇T_e (middle), $\nabla V\phi$ and ∇T_i (bottom). The data in the XICS panel is focused on the very core region ($\rho \sim 0.2$) and cover the full ECH injection period and some time before and after ECH. CES data is come from several positions (ρ from 0.2 to 0.5) and several time points.

accompanied by a reduction in $\mathrm{d}V_\phi/\mathrm{d}r$ is apparent. Just as the first pair of figures was the ECH analogue of the macroscopic Rice scaling, this pair is the analogue of previous local intrinsic rotation studies which showed the correlation between $V_\phi(0)$ and pedestal $\mathrm{d}T_i/\mathrm{d}r$ [22, 23]. The third pair of plots in figure 6 shows the change (NBI versus NBI + ECH) in $\mathrm{d}V_\phi/\mathrm{d}r$ versus $\mathrm{d}T_i/\mathrm{d}r$. In this case, the scatter is larger. Still, the data indicates that the flattening of $\mathrm{d}V_\phi/\mathrm{d}r$ is accompanied by a reduction in $\mathrm{d}T_i/\mathrm{d}r$ along with an increase in $\mathrm{d}T_e/\mathrm{d}r$. This suggests that the appearance of the ECH-induced counter-torque is accompanied by a change in the species which stores the preponderance of free energy. All told, figure 6 strongly suggests that the ECH-induced counter-intrinsic torque is ∇T_e driven.

The correlation of $\Delta\nabla V_\phi$ with $\Delta\nabla T_e$, and our cognizance of the theoretical prediction that a change in mode propagation direction can change the sign of the residual stress Π^R and hence that of the intrinsic torque density $\tau = -\partial_r \Pi^R$, lead us to investigate other ECH-induced changes which may signal a tip of the system towards the electron channel. Figure 8(c) shows the collision frequency plotted versus ρ for NBI-only and NBI + ECH. Rather clearly, ECH triggers a drop in ν_{*e} by a factor 2–3. In the NBI + ECH cases, electron collisions are still non-negligible, but TEMs are surely possible. As the TEM frequency and growth depend heavily on ∇n, we
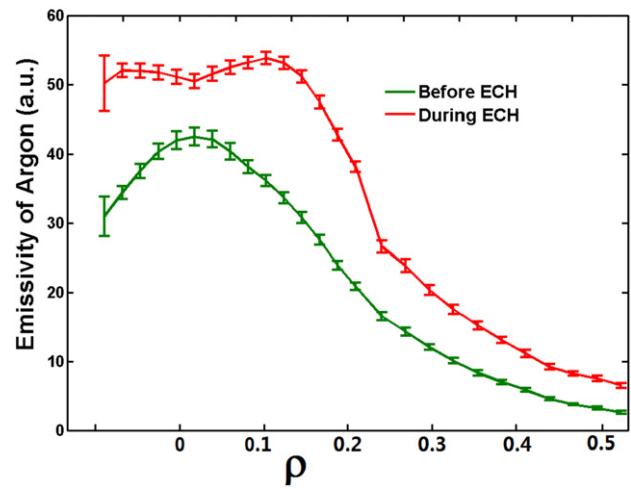

Figure 7. The emissivity profiles of helium-like argon.

should also look for a density profile change with ECH. No core density profile information is available for KSTAR. We found the line-averaged density always increases slightly when on-axis ECH is injected in KSTAR. Moreover, the profile of Argon radiation measured with XICS is also indirect evidence
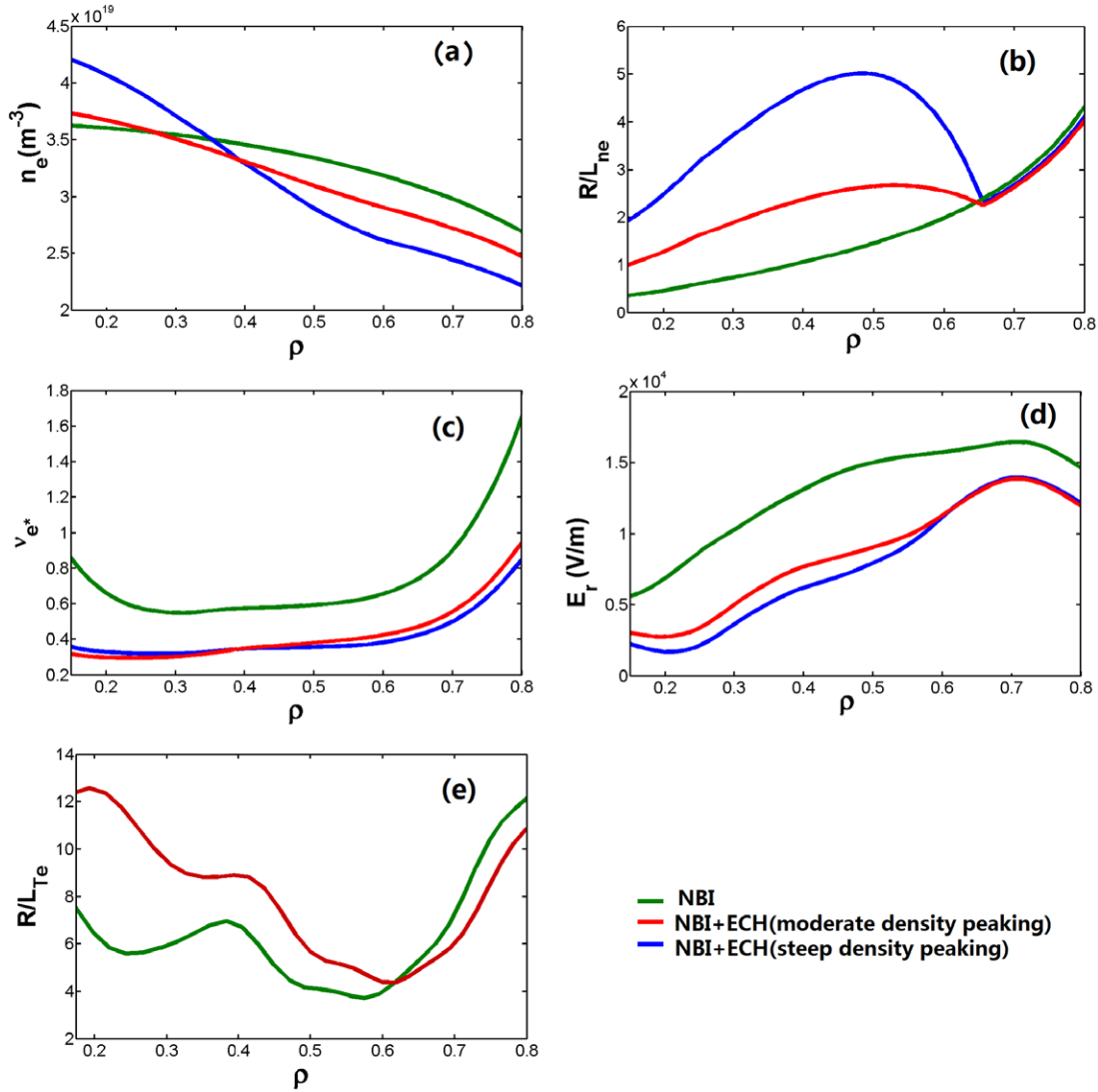
Figure 8. (*a*) Synthetic density profile, (*b*) normalized inverse gradient scale length of density (*c*) effective collision frequency, (*d*) $E \times B$ shearing rate, (*e*) normalized inverse gradient scale length of T_e.

for density peaking during the injection of ECH (as shown in figure 7). The helium-like argon will be burn out in the core region when T_e is higher than 3 keV. This means that the intensity profile measurement with XICS should become hollow at higher T_e. On the other hand, the sightline of XICS on KSTAR is across the NBI path, which can produce quite a few helium-like argon ions and make the peaking emissivity profile helium-like Argon of XICS even with very high T_e. There are two main characters in figure 7. Firstly, the emissivity profiles become a little hollow inside $\rho \sim 0.1$ during ECH injection which is the effects of T_e to background helium population. Secondly, the overall emissivity profiles become more peaked during injection of ECH. With higher T_e, the helium-like argon become more peaked, the density peaking is the most likely reason. Indications from measurements of line-averaged density are that some ∇n peaking occurs, as in similar experiments elsewhere [13]. Based on the line-averaged data and impurity profiles, we have constructed a range of possible 'synthetic' $n(r)$ profiles which are shown in figure 8(*a*).

4. Analysis and interpretation

The drop in collisionality, the steepening of ∇T_e and slight drop in ∇T_i, the indirect evidence that ∇n steepens, and the correlation of $\Delta \nabla V_\phi$ with $\Delta \nabla T_e$ as NBI $\rightarrow$ NBI + ECH all together suggest the hypothesis that a TEM-driven core counter-torque acts to modify the KSTAR rotation profiles. Noting that theory and simulation predict that residual stress can change sign as the turbulence flips from ITG $\rightarrow$ TEM (i.e. $V_{*i} \rightarrow V_{*e}$, so the direction of V_{gr} changes, where V_{gr} is the radial group velocity of the waves [4].) and that ∇T_e can drive a residual stress via TEM [24], we now investigate the evidence for a change in the direction of the turbulence-driven torque. Three issues arise—first, the dynamics of ∇n peaking must be understood. This is important since ∇n steepening reduces η_i and so works against ITG and for TEM. More generally, this tells us that the particle and momentum channels are strongly coupled. Second—the mechanism of symmetry breaking in the TEM residual stress must be identified. Electric field shear is quite modest in the core of KSTAR, so the

viability of the conventionally invoked mechanism is unclear. Third—is there actual quantitative evidence for the change in character of the underlying micro-turbulence? We address these issues here. Regarding the first, the unavailability of density profile information makes any substantive work impossible. Similarly, without the $n_e(r)$ profile, no progress on impurity profile effects is possible. Thus, we are limited only to exploring a range of synthetic density profiles which are shown in figure 8(a). Figure 8(b) shows the gradient of density profiles used in the GS2 analysis. R/L_{n_e} at $\rho = 0.5$ are 1.45, 2.65, 4.99 depending on the profiles. We note that these values are very similar to R/L_{n_e} at $\rho = 0.45$ in AUG [13, 25, 26]. We note that recent simulation articles suggest that ECH-induced density peaking occurs in a 'mixed state' of TEM and ITG turbulence by a combination of reduced outward convection and an increase in inward thermo-diffusion [25, 26]. Regarding the second, direct measurement of the structure of the residual stress is not possible, except by HIBP or edge Langmuir probes. Hence, we are limited to inferences based on indirect macroscopic evidence. Regarding the third, nonlinear gyrokinetic simulation of rotation profile evolution is beyond the capability of present day codes. Thus, we perform linear gyrokinetic stability analysis of experimentally determined profiles, so as to compare results for NBI-only plasmas (i.e. 'before') with NBI + ECH (i.e. 'after') plasmas. Results which address the second and third issues are presented below.

Here we address symmetry breaking and the structure of the residual stress. Regarding symmetry breaking, figure 8(d) shows a comparison of $E \times B$ velocity (V_E) profiles for NBI only and NBI + ECH cases. To obtain V_E, radial force balance is used, where $T_i(r)$ and $V_\phi(r)$ are measured, $n(r)$ is synthesized (though constrained by line-averaged data) and $V_\theta(r)$ is calculated, assuming neoclassical rotation. Plots indicate that V_E actually decreases with ECH, due to the increase in n and the flattening of $V_\phi(r)$. V_E' is roughly constant. This outcome is in distinct contrast to the case of ETBs or ITBs, where the increase in intrinsic torque is accompanied by an increase in V_E'. In contrast, figure 8(e) compares a plot of $1/L_{T_e}$ 'before' and 'after'. Clearly, $1/L_{T_e}$ increases with ECH. Now, we also note that L_{T_e} is effectively an upper bound on the turbulence intensity gradient scale, set by the scale $L_I = (\partial_r I/I)^{-1}$, where I is the local fluctuation intensity. Recall that a finite intensity gradient *breaks spectral* $\langle k_\theta k_\| \rangle$ symmetry by yielding a finite dispersion in $k_\|$ [4, 27]. Thus, we see that the strength of symmetry breaking by intensity gradient actually *increases* with ECH, giving a positive feedback loop. This leads us to analyse the implications of that mechanism for ECH-induced intrinsic torque. A gyrokinetic calculation of the residual stress $\Pi_{r\phi}^R$ for CTEM turbulence gives the prediction that [28]:

$$\Pi_{r\phi}^R = 2\frac{\Omega_i}{L_I}\frac{\hat{s}}{Rq}\sum_{\underline{k}} \tau_{c\underline{k}} k_\theta^2 \varrho_s^2 c_s^2 x^2 \left|\frac{e\hat{\phi}_k}{T_e}\right|^2 \left(1 + 2\tau + 4\tau^2\frac{L_n}{R_0}\right). \tag{1}$$

Here, $L_I^{-1} = (1/I)(\partial I/\partial r)$ is the intensity gradient scale length, $\tau = T_i/T_e$, $x = r - r_{0m,n}$ with $r_{0m,n}$ is the radial location of the resonance surface, and $\tau_{c\underline{k}}$ is the correlation time. We use the mixing length estimation for turbulence intensity, $I \sim (l_c/L_{T_e})^2$ with l_c is the correlation length, and

so $1/L_I \sim 2/L_{T_e}$ is used in deriving equation (1) (we didn't assume $L_I \sim L_{T_e}$ directly). The distinction between parallel and toroidal is ignored in Π^R. Then taking $L_I \sim L_{T_e} > 0(L_{T_e} \equiv -(1/T_e)(\partial T_e/\partial r)$, using the mixing length estimate $I \sim (l_c/L_{T_e})^2$ so $1/L_I \sim 2/L_{T_e}$, performing the spectral sum, and balancing CTEM residual stress with diffusion give:

$$\Delta\left(\frac{\partial\langle v_\phi\rangle}{\partial r}\right) \cong 2\Omega_i\frac{\Delta^2}{L_{T_e}}\frac{\hat{s}}{Rq}\left(1 + 2\tau + 4\tau^2\frac{L_n}{R_0}\right) \tag{2}$$

Δ is the radial spectral width. Equation (2) gives the change in $\partial\langle v_\phi\rangle/\partial r$ induced by CTEM intrinsic torque. Note $\Delta\left(\partial\langle v_\phi\rangle/\partial r\right) > 0$ consistent with the observed rotation profile flattening. We have absorbed the difference between the turbulence in the NBI only (i.e. ITG) state and the NBI + ECH state (i.e. ITG + TEM mixed or TEM state) into the factor $\tau_{c\tilde{k}}\langle\tilde{v}_r^2\rangle_{\tilde{k}}$, where $\tilde{v}_{r\tilde{k}} = k_\theta\rho_s c_s e\tilde{\phi}_{\tilde{k}}/T_e$. Note that this factor is common to both the residual stress Π^R and the momentum diffusivity χ_ϕ, and so cancels out of the ratio Π^R/χ_ϕ, which appears in equation (2). Thus equation (2) constitutes a satisfactory approximation for the change in $\partial\langle v_\phi\rangle/\partial r$. To accurately distinguish the effects of between NBI and NBI + ECH mixed state of TEM + ITG requires understanding of the change in fluctuation spectrum, which is far beyond the linear stability analysis described here. Thus, the effect of the external torque does not enter $\Delta\left(\partial\langle v_\phi\rangle/\partial r\right)$. In reality, the external torques from NBI for CTEM and ITG are comparable, but $\chi_\phi^{CTEM} \neq \chi_\phi^{ITG}$, so corrections should be considered. The key point concerning equation (2) is that $\Delta\left(\partial\langle v_\phi\rangle/\partial r\right) \sim 1/L_{T_e}$, consistent with the results of the middle panel (XICS) in figure 6. Finally, keep in mind that necessarily $L_I < L_{T_e}$, so equation (2) gives a lower bound on the strength of the CTEM-induced counter-torque.

Regarding the third issue in the above section, we analysed the change in linear micro-instability caused by ECH injection using the flux tube gyrokinetic code GS2. We compared the linear stability of the plasma profiles for NBI only to those of the plasma profiles for NBI + ECH including electron and ion collisions, $E \times B$ shearing, and toroidal rotation. We used the ion temperature and rotation profiles measured by CES and the electron temperature profiles by ECE. Without any measured density profile, we synthesized one as follows. The density profile at the time with NBI only is assumed to take the form $n_e(\rho) = (n_e(0) - n_e(1)) \times (1 - \rho^2)^{0.4} + n_e(1)$, $n_e(1) = 0.15 \times n_e(0)$. Here, ρ represents a radial coordinate defined as $\rho = \sqrt{\psi/\psi_x}$ for the poloidal magnetic flux ψ and ψ_x *is* the flux value at last closed flux surface. After ECH injection, the profile of Ar emissivity indicates moderate density peaking. As shown in figure 8(a), two cases for density peaking during ECH injection are assumed. One is moderate peaking profile. The other is a sharp peaked profile. The profiles for ECH phase are assumed to be of the form:

$$n_e(\rho) = n_{e1}(\rho) + n_{e2}(\rho) \tag{3}$$

$$n_{e1}(\rho) = (n_{e1}(0) - n_{e1}(1)) \times (1 - \rho^2)^{0.4} + n_{e1}(1) \tag{4}$$

$$n_{e2}(\rho) = n_{e2}(0)) \times (1 - (\rho/\rho_0)^2)^2. \tag{5}$$

For the moderate density peaking case in figure 8(a), $n_{e1}(1) = 0.19 \times n_{e1}(0), n_{e2}(0) = 0.15 \times n_{e1}(0)$. For the sharp density peaking case, $n_{e1}(1) = 0.17 \times n_{e1}(0)$,
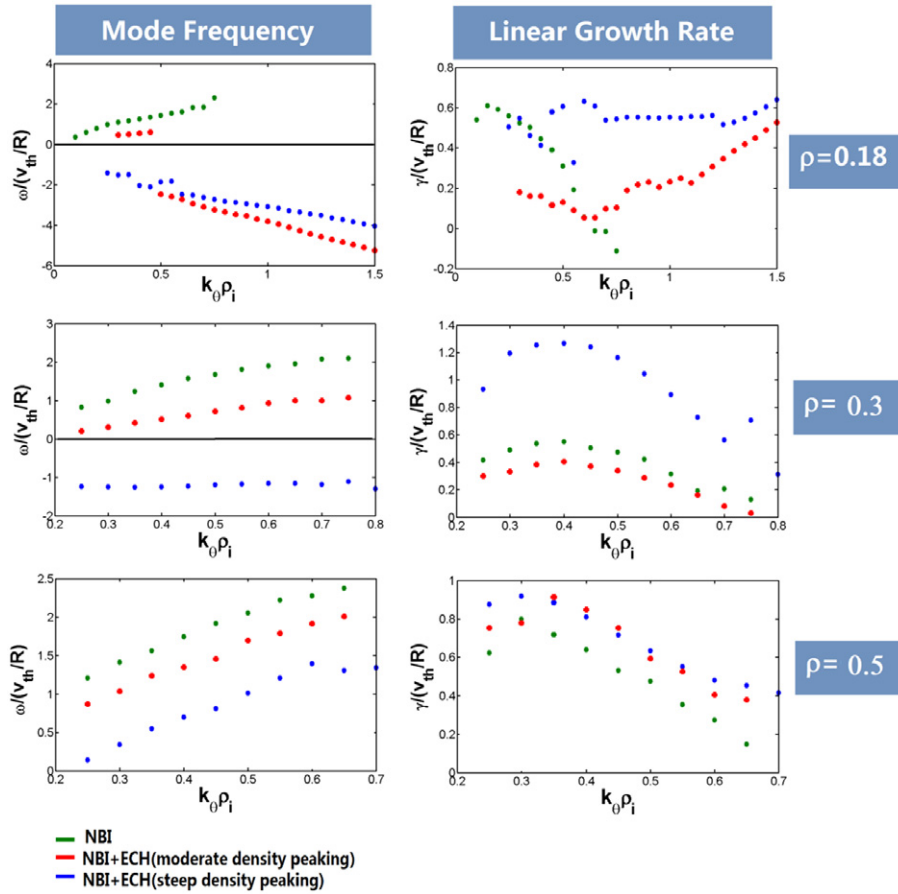
Figure 9. Mode frequency and linear growth rate simulated with GS2 at three positions ($\rho = 0.18$, 0.3 and 0.5).

$n_{e2}(0) = 0.47 \times n_{e1}(0)$. And $n_{e2}(\rho) = 0$ if $\rho \geqslant \rho_0$. The line-averaged density values were used to find $n_e(0)$ and $n_{e1}(0)$. Based on the Ar emissivity profile, we chose $\rho_0 = 0.6$. Based on the observation that the toroidal rotation change occurs inside ρ_{pivot}, with $\rho_{pivot} = 0.7$ as a pivot point, we chose three different radial positions ($\rho = 0.18$, 0.3 and 0.5) for the analysis of the variation of the dominant micro-instabilitiy growth.

Before ECH injection, the plasma profiles support ITG (ITG Ion Temperature Gradient Instability) in the $\rho < 0.6$ region, as we can see in figure 9 (green dots). First, let's focus on the moderate density peaking case. During ECH injection, TEM (trapped electron mode instability) become unstable for high $k_\theta > 0.5$ in deep core ($\rho = 0.18$), due to relatively moderate density gradients (figure 9 red dots). Note that negative frequencies here correspond to propagation in the electron diamagnetic direction. The increase in electron temperature and its steepened gradient lead to the excitation of TEM in the deep core ($\rho = 0.18$) after the ECH injection. We can see that for wave numbers $k_\theta > 0.5$, a change of micro-instabilities occurs i.e. ITG $\rightarrow$ TEM. In other regions, ECH injection causes little change—the dominant mode is still ITG, albeit with reduced frequencies and growth rates. When the density is more peaked (sharp peaking case in figure 8(*a*)), it can be seen that the change of micro-instabilities occurs for the whole range of wave numbers at $\rho = 0.18$ and $\rho = 0.3$. Compared to the conservative density peaking case, the mode

flip is clear in the core region. On the other hand, the range of excitation of TEM is still limited to deep core even for sharp peaking case. Thus, a problem emerges, namely that the popularly favoured hypothesis is not supported by the data. To address this issue, we remark that fluctuation intensity can spread beyond the linearly unstable region by nonlinear scattering processes such as turbulence spreading and heat avalanches [29], etc. Thus, resolving the physical problem may require consideration of non-locality processes. Also, the limited extent of the region where the dominant micro-instability changes suggests that the state of turbulence in neighbouring radial regions is very likely a dynamic, evolving mixture of both ITG and TEM turbulence. The mixed state of ITG and TEM is also proposed in [14] for AUG experiment. The ideas of mixed states of both TEM and ITG, and the extension of TEM influence with nonlinear processes are shown in the simple cartoon in figure 10. The intrinsic torque from this mixed population of ITG and TEM will be determined by the competition between different spectral components of the momentum flux, and may not be possible to calculate within a simple quasi-linear approach. Detailed study of this process requires global nonlinear simulation and more detailed modelling, which are subjects for future work. We remark here that this rather unsatisfactory result dramatizes the need for accurate measurement of density and impurity profiles, and for spatially localized heterodyne fluctuation measurements in coordination with macroscopic profile studies.
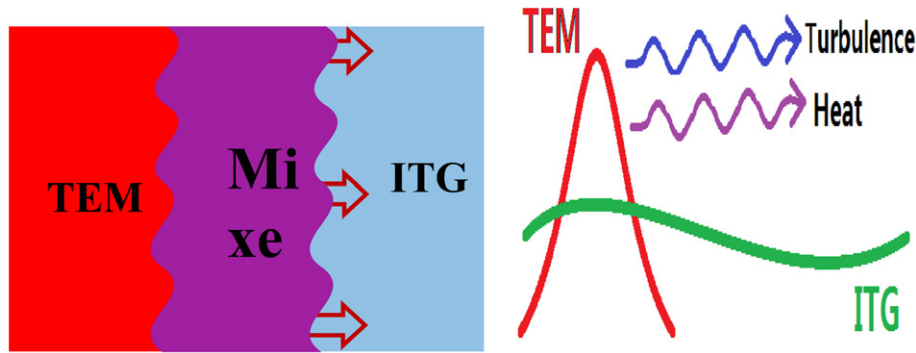
Figure 10. Cartoons showing the mixed states (left) and extension of TEM influence with nonlinear processes (right).

5. Summary, discussion and future plans

ECH induces a counter-current rotation increment in the L-mode and H-mode co-NBI plasmas studied so far. Both XICS and CES confirm that the core toroidal rotation dramatically decreases when a modest amount of on-axis ECH is injected to H-mode plasmas. Both the change of rotation and its gradient have a close relation to the change of electron temperature and its gradient in the core plasma. However, analyses show that the popular, simple explanation of the intrinsic counter-torque as a consequence of the turbulence 'flipping' from ITG $\rightarrow$ TEM is somewhat problematic. First, the symmetry breaking mechanism for the residual stress needs to be clarified. We offer intensity gradient as a relevant improvement over $\langle V_E \rangle'$, but further work is needed. Second, gyrokinetic micro-stability analysis using experimental profiles indicates that and region of mode flip transition is very sensitive to the density peaking. More peaked density profiles favourite a broader mode flip region. Third, the ITG $\rightarrow$ TEM flip is limited only to the deep core ($\rho < 0.2$–0.3), while the intrinsic torque has an impact for all $\rho \leqslant \rho_{\mathrm{piv}} \sim 0.7$. Thus, certainly a mixed state will occur, and consideration of turbulence propagation or other type of non-local effect may be required. Density profile evolution is clearly critical to this study, and a satisfactory explanation of the peaking phenomenon is as yet elusive. Momentum and particle transport are coupled and must be studied together.

The other possible mechanism for the counter-current rotation induced by ECH is a neoclassical toroidal viscosity (NTV) effect [30]. Indeed, some weak $n:m = 1:1$ kink mode appeared when ECH was injected in KSTAR 2011's campaign. For the ECH + NBI plasma in KSTAR, we don't think NTV is the main source of torque. There are two pieces of experiment evidence in KSTAR which don't support by the NTV hypothesis. One is the experimental results of off-axis ECH heating. The toroidal rotation still decreases when the resonance layer of ECH is far from the $q \sim 1$ surface. The new ECH + NBI rotation results in 2012 show that there is no $1:1$ kink mode in many discharges when ECH is injected to NBI plasma, but toroidal rotation still decreases.

For the future research, we will revisit various physics issues addressed in this work with refined measurements, especially density profile. With these refined profiles,

improved gyrokinetic analysis result will be compared with core fluctuation measurement using BES system, which will clarify the ITG versus TEM issues addressed in this work.

References

[1] Rice J.E. *et al* 2007 *Nucl. Fusion* **47** 1618
[2] Ida K. *et al* 1991 *Nucl. Fusion* **31** 943
[3] Rice J.E. *et al* 1998 *Nucl. Fusion* **38** 75
[4] Diamond P.H. *et al* 2008 *Phys. Plasmas* **15** 012303
[5] Gurcan O.D. *et al* 2007 *Phys. Plasmas* **14** 042306
[6] Kwon J.M. *et al* 2012 *Nucl. Fusion* **52** 013004
[7] Camenen Y. *et al* 2011 *Nucl. Fusion* **51** 073039
[8] Bortolon A. *et al* 2006 *Phys. Rev. Lett* **97** 235003
[9] Rice J.E. *et al* 2011 *Phys. Rev. Lett* **107** 265001
[10] Ida K. *et al* 2001 *Phys. Rev. Lett* **86** 3040
[11] deGrassie J.S. *et al* 2004 *Phys. Plasmas* **11** 4323
[12] Yoshida M. *et al* 2009 *Phys. Rev. Lett.* **103** 065003
[13] McDermott R.M. *et al* 2011 *Plasma Phys. Control. Fusion* **53** 035007
[14] Angioni C. *et al* 2011 *Phys. Rev. Lett.* **107** 215003
[15] Lee G.S. *et al* 2000 *Nucl. Fusion* **40** 575
[16] Lee S.G. *et al* 2010 *Rev. Sci. Instrum.* **81** 10E506
[17] Ko W.H. *et al* 2010 *Rev. Sci. Instrum.* **81** 10D740
[18] Jeong S.H. *et al* 2010 *Rev. Sci. Instrum.* **81** 10D922
[19] Bae Y.S. *et al* 2012 *Fusion Eng. Des.* **87** 1597
[20] Bae Y.S. *et al* 2012 Status and near plan of KSTAR heating and CD devices *2012 KSTAR Conf. (Muju, Korea, 2012)* http://kstar.nfri.re.kr/kstarweb/upload/kboard/O.4.3_KSTAR_HCD_status_plan(20120223)_f2.pdf
[21] Diamond P.H. *et al* 2009 *Nucl. Fusion* **49** 045002
[22] Ida K. *et al* 2010 *Nucl. Fusion* **50** 064007
[23] Rice J.E. *et al* 2011 *Phys. Rev. Lett.* **106** 215001
[24] Wang W.X. *et al* 2011 *Phys. Rev. Lett.* **106** 085001
[25] Fable E. *et al* 2010 *Plasma Phys. Control. Fusion* **52** 015007
[26] Angioni C. *et al* 2011 *Nucl. Fusion* **51** 023006
[27] Gurcan O.D. *et al* 2010 *Phys. Plasmas* **17** 032509
[28] Wang L. *et al* 2013 *Phys. Rev. Lett.* **110** 265006
[29] Gurcan O.D. *et al* 2005 *Phys. Plasmas* **12** 032303
[30] Shaing K.C. 2003 *Phys. Plasmas* **10** 1443